JACS
JOURNAL OF THE AMERICAN CHEMICAL SOCIETY

Article

pubs.acs.org/JACS

From Planar to Cage in 15 Easy Steps: Resolving the $C_{60}H_{21}F_9^- \rightarrow C_{60}^-$ Transformation by Ion Mobility Mass Spectrometry

Jean-François Greisch,[‡] Konstantin Yu. Amsharov,[*,§] Jürgen Weippert,[†] Patrick Weis,[†] Artur Böttcher,[†] and Manfred M. Kappes[*,†,‡]

[†]Institute of Physical Chemistry, Karlsruhe Institute of Technology (KIT), Fritz-Haber-Weg 2, 76131 Karlsruhe, Germany

[‡]Institute of Nanotechnology, Karlsruhe Institute of Technology (KIT), Hermann-von-Helmholtz-Platz 1, 76344 Eggenstein-Leopoldshafen, Germany

[§]Institut für Organische Chemie, University Erlangen-Nürnberg, Henkestrasse 42, 91054 Erlangen, Germany

Supporting Information

ABSTRACT: A combination of mass spectrometry, collision-induced dissociation, ion mobility mass spectrometry (IM-MS), and density functional theory (DFT) has been used to study the evolution of anionic species generated by laser-desorption of the near-planar, fluorinated polycyclic aromatic hydrocarbon (PAH), $C_{60}H_{21}F_9$ (s). The dominant decay process for isolated, thermally activated $C_{60}H_{21}F_9^-$ species comprises a sequence of multiple regioselective cyclodehydrofluorination and cyclodehydrogenation reactions (eliminating HF and H_2, respectively, while forming additional pentagons and/or hexagons). The DFT calculations allow us to set narrow bounds on the structures of the resulting fragment ions by fitting structural models to experimentally determined collision cross sections. These show that the transformation of the precursor anion proceeds via a series of intermediate structures characterized by increasing curvature, ultimately leading to the closed-shell fullerene cage C_{60}^- as preprogrammed by the precursor structure.

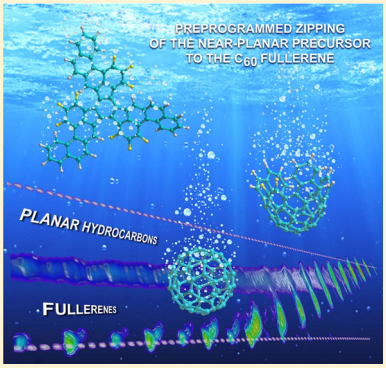

INTRODUCTION

Numerous experiments performed over the past two decades have pointed out the unique potential of polycyclic aromatic hydrocarbons and their halogenated derivatives (X-PAHs; X = F, Cl, Br), for the generation of novel carbon nanostructures via selective chemical transformations. This has implications for diverse fields ranging from nanotechnology to astronomy.

Examples of unimolecular PAH and X-PAH transformation reactions include regioselective intramolecular cyclodehydrogenation and in particular synchronous cyclodehydrohalogenation processes.[1,2] These can lead to shortening of molecular perimeters via additional carbon ring formation[1,2] together with a substantial increase of PAH curvature. The underlying reactions typically require significant activation energy. We have recently shown that energization by electron-impact can be used for this purpose.[3] More conventionally, the transformation is activated thermally, e.g., by flash vacuum pyrolysis (in the gas phase) or laser-induced desorption or by heating precursors on (catalytically active) surfaces under ultrahigh vacuum conditions.[4,5]

When heating appropriately designed quasiplanar PAH adsorbates on atomically clean flat surfaces, a sequence of such thermally activated on-surface cyclodehydrogenations can lead to increasing curvature and associated strain sufficient to cause carbonaceous caps to form. For example, scanning tunneling microscopy has shown that thermal activation of quasiplanar precursors on a Pt(111) surface can lead to carbon hemispheres.[6] Such caps appear to be useful for carbon nanotechnology: evidence has recently been obtained that cap-like PAH derivatives can nucleate the selective growth of isomer pure single-walled carbon nanotubes (SWCNTs) by chemical vapor deposition (CVD).[7]

Conversion of planar PAHs into three-dimensional sp^2-carbon frameworks is also of interest in the context of fullerene cage formation. For example, several recent studies have demonstrated that laser-desorption of polydisperse PAH-related carbonaceous materials such as asphaltenes generates fullerene cages.[8,9] On a much larger scale, the astronomical observation of interstellar C_{60} and C_{60}^+ has led to a renewed focus on possible fullerene formation routes in the gas phase, including elementary reactions which can convert large PAHs into carbon cage structures.[10] Compared to PAH → cap conversion, fullerene formation can result from an analogous, but more prolonged, sequence of regioselective intramolecular cyclizations. In a pioneering experiment, laser-induced desorption/fragmentation of $C_{60}H_{30}$, a planar carbon framework with a structure designed to transform to C_{60} by such a cyclization cascade, was shown to indeed generate small amounts of C_{60}.[11] The same authors demonstrated that the C_{60} yield could be increased by flash vacuum pyrolysis of $C_{60}H_{27}Cl_3$, an X-PAH derivative comprising the same carbon

Received: June 16, 2016
Published: August 8, 2016

DOI: 10.1021/jacs.6b06205
J. Am. Chem. Soc. 2016, 138, 11254−11263

framework as $C_{60}H_{30}$.[12] Subsequently, it was suggested that the conversion yield could be increased even further by using analogous F-PAHs, with fluorine and hydrogen atoms in alternate positions allowing the concerted closure to the fullerene cages via a "preprogrammed" sequence of regioselective intramolecular cyclizations associated with facile HF- (and some subsequent H_2-) losses.[13] Support for this concept has recently been obtained in a mass spectrometric study of the charged fragments generated by laser ablation/desorption of the near-planar F-PAH precursor, $C_{60}H_{21}F_9$. Both C_{60}^+ and C_{60}^- ions can be resolved in the corresponding fragment mass spectra in significant amounts,[14] leading to the further proposition that the same overall approach could be used for the targeted generation of other fullerenes, via the synthesis of appropriate "structurally programmed" precursors which transform into the desired cage upon sufficient energization.[15]

Recent progress in the synthesis of large PAH derivatives allows the preparation of a wide range of near-planar F-PAH precursors with F and H atoms located precisely at the positions required for preprogrammed HF/H_2-elimination to generate targeted nanostructures by heating.[14] In combination with catalytically active alumina substrates, multi-milligram quantities of "buckybowl" products have already been obtained in this way.[16] Nevertheless, the rational synthesis of fullerenes on a comparable scale still remains challenging. The main limitations to be overcome are the complexity of the precursor synthesis, the coexistence of multiple fragmentation products in the case of incomplete elimination, as well as solubility issues.[1] Correspondingly, while ^{13}C labeling in combination with mass spectrometry has clearly demonstrated that only one $C_{60}H_{21}F_9$ precursor molecule is involved in the formation of a given $C_{60}^{\pm}$ species detected after laser-desorption,[17] there has been no spectroscopic confirmation that closed-shell $C_{60}(I_h)$ (rather than other less compact isomers of C_{60}) is actually generated in the transformation. Similarly, upon surface mediated pyrolysis,[18] the near-planar precursors deposited on Pt-group metal surfaces have been shown to yield compact fullerene- and/or dome-like species whose overall topology can be verified by STM but whose atomic structure could not be resolved.[19−21]

Previous work on the transformation of PAHs and X-PAHs into caps and cages has so far been directed more toward proof-of-principle experimental demonstration and nanotechnological applications, rather than toward understanding and quantifying the associated transformation mechanisms. In particular, little is known about the energetics, transition states, and other kinetic aspects of the individual reaction steps. As a result, there is currently no general theoretical description which could be used to predict (and further enhance) the yield of the HF/H_2-elimination cascade as a function of the variables: starting molecular geometries, excitation energy, and competing dissipation/decay processes. In this context, it would be informative to experimentally follow the elimination cascade from precursor to fullerene for a large F-PAH benchmark system, obtaining structural and thermodynamic information at each step along the fragmentation path.

For this purpose we have measured the ion mobility (and collisional cross sections) of all mass spectrometrically distinguishable anionic species generated by laser-desorption of solid $C_{60}H_{21}F_9$, at various desorption laser fluences sufficient to produce C_{60}^-. These experiments were accompanied by systematic DFT-based calculations which reconstruct the experimentally determined collisional cross sections of the fragment anions and thus allow their structural assignment (via a fit to the mobility data). We confirm that the dominant fragmentation reactions which give rise to anionic products consist of a series of HF- and H_2-eliminations and conclusively show that these systematically increase the curvature of the carbon core. Ultimately, a sequence of 15 elimination steps (in multiple possible combinations of nine HF- and six H_2-eliminations) yields a closed-shell carbon cage with 60 atoms. By performing additional collision-induced dissociation studies we also demonstrate that this 15 step sequence occurs fully in the gas phase and therefore comprises a cascade of only unimolecular reactions; i.e., on-surface fragmentation and (re)association processes are insignificant as sources for C_{60}^- under our laser-desorption conditions.

EXPERIMENTAL METHODS

The ion mobility measurements were performed on a SYNAPT G2-S HDMS (Waters Corporation, Manchester, U.K.) traveling-wave ion mobility[22] mass spectrometer (TWIMS) equipped with a laser-desorption ionization source operated in negative ion mode. This family of instruments is characterized by a high transmission efficiency and a separative power comparable to that of moderate resolution ($\Delta t/t \approx 20-50$) conventional drift cells.[23]

Prior to analysis, the $C_{60}H_{21}F_9$ powder (prepared according to the procedure described in ref 9) was smeared onto a sandblasted microscope slide which was itself mounted on a metal holder. The compound was then laser-desorbed/ionized using 355 nm nanosecond laser pulses characterized by an about 150 mJ/cm^2 maximal fluence, an about 10^{-4} cm^2 elliptic spot size, and a repetition rate of 2.5 kHz. The sample was continuously moved at maximal available speed to ensure the refreshment of the material to be desorbed. Under these conditions, the fluence threshold for laser-desorption ionization was estimated to be slightly below 70 mJ/cm^2 for the compound studied. In the first set of experiments, all ions generated by laser-desorption were first (softly) accumulated in a trapping ion guide filled with argon prior to release and injection though a helium curtain into the traveling-wave ion mobility cell (N_2 pressure of about 2.8 mbar). Following ion mobility separation, the ions were guided to an orthogonal acceleration time-of-flight mass analyzer (>10^4 fwhm mass resolution). The reported data corresponds to optimized traveling waves of 40 V with velocities of 650 m/s. No correction has been implemented in the displayed arrival time distributions for the time spent by the ions between their departure out of the ion mobility cell and detection (estimated to be less than 0.05 ms). Although the separation characteristics of traveling-wave ion mobility cells have been shown to be similar to those of conventional drift tube devices, the relationship between measured arrival times and mobility is different.[23] In the present work, comparison with computed structures was achieved using a combination of internal and external references of known cross sections as described in the next section.

In the second set of experiments, we have explored the fragmentation behavior of desorbed ions by subsequently activating them collisionally (collision-induced dissociation (CID)). For this, laser-desorbed parent ions were first mass selected with a quadrupole-mass-filter and then injected (with variable energy) into the trapping ion guide filled with Ar to a pressure of 2.3×10^{-2} mbar. The emerging fragment ions were then analyzed with respect to their structure and mass by combining traveling-wave ion mobility spectrometry with time-of-flight mass analysis as described above. Additional details are provided as Supporting Information.

COMPUTATIONAL METHODS

Quantum chemical calculations were performed with the TURBOMOLE program package.[24] The geometry parameters of the different $C_{60}H_xF_y^-$ species were fully optimized at the BP86 level[25,26] with the def-svp basis set.[27] For each structure, the collision cross section (CCS) was calculated with the projection approximation (PA)[28] as implemented in the mobcal program package.[29] Since mobcal describes cross sections for static drift tube measurements with helium

DOI: 10.1021/jacs.6b06205
J. Am. Chem. Soc. 2016, 138, 11254−11263

as buffer gas while our experiments were performed in nitrogen with a traveling-wave spectrometer, a calibration procedure is required. For this we measured the maxima of the arrival time distribution (ATD) of $C_{60}H_{21}F_9^-$ and C_{60}^- (8.8 and 4.5 ms, respectively), see Figure 4 and Supporting Information Figure S1. The corresponding C_{60}^- signal was obtained by laser-desorption of solid fullerene-$C_{60}(I_h)$. ATD values depend on instrumental parameters such as nitrogen pressure and temperature, as well as traveling-wave speed and amplitude which were kept constant throughout the experiment. From the known structures of $C_{60}H_{21}F_9$ and $C_{60}(I_h)$ we first calculated their collision cross sections in helium by the projection approximation[28,29] (PA-CCS, 230 and 120 Å^2, respectively) and then determined the parameters of the linear calibration curve which connects the latter PA-CCS values to their experimental ATD maximum in nitrogen (ATD_{PA}[ms] = 0.0395 × PA-CCS [Å^2] − 0.24 [ms]). (The CCS is to first order proportional to the drift time in the ion mobility cell.[22] The ATD consists of the sum of drift time and a constant offset comprising the time the ions spend in the mass spectrometer, ion transfer, and trigger delays.) On the basis of this calibration, we have transformed the PA-CCS for every calculated structure into an arrival time directly comparable to the experimental value. A candidate structure is deemed plausible if its arrival time agrees to within 5% with the experiment. This confidence interval was estimated from the experimental error (<2%), the known limitations of computed DFT structures, the projection approximation used to compute the cross section, and the calibration procedure. For completeness we have also included collision cross sections based on the more sophisticated trajectory method (TM)[30] as implemented in the mobcal package. Since the TM-CCS of $C_{60}H_{21}F_9$ and $C_{60}(I_h)$ are slightly larger (235 and 125 Å^2, respectively), the linear calibration curve that connects the TM-CCS values to ATD maxima calculates to ATD_{TM} [ms] = 0.0396 × TM-CCS [Å^2] − 0.46 [ms]. Note that our inferences below are independent of the two procedures (PA or TM) used to calculate collision cross sections.

RESULTS AND DISCUSSION

Mass spectra obtained upon laser-induced desorption/ionization of $C_{60}H_{21}F_9$ were recorded in the negative ion channel. Relative mass spectral intensities depend critically on the laser power. As can be seen from Figure 1, the dominant fragments of $C_{60}H_{21}F_9^-$ (m/z = 912) are $C_{60}H_{20}F_8^-$, $C_{60}H_{19}F_7^-$, and $C_{60}H_{18}F_6^-$; i.e., we observe a series of selective sequential HF-losses (Δm = 20). Even at low laser power, this fragmentation cascade can be followed all the way down to $C_{60}H_{12}^-$ (see Figure 1a, black arrows). In the lower mass range, the (partially competing) H_2-loss channel leading to $C_{60}H_{21-x-2y}F_{9-x}^-$ increases in relative intensity (see Figure 1a, red, blue, and green arrows, corresponding to y = 1,2,3). Increasing the laser power (Figure 1b) leads to increased fragmentation: (i) C_{60}^- (m/z = 720) becomes more prominent, and (ii) additional species are observed below m/z = 720; here the fragmentation cascade changes to C_2-loss (Δm = 24) leading to C_{58}^- (m/z = 696), C_{56}^- (m/z = 672), C_{54}^- (m/z = 648), C_{52}^- (m/z = 624), and C_{50}^- (m/z = 600). This C_2-loss sequence is characteristic of fullerenes, see Figure S1, and is in itself a strong indicator that fullerenes are formed upon laser irradiation/desorption of $C_{60}H_{21}F_9$ via HF and H_2-loss. Note, however, that at high laser power HF/H_2-loss is not the only channel: we also observe addition of fluorine atoms (leading to a peak at m/z = 931, possibly due to accretion in the laser-desorption plume) as well as loss of odd numbers of hydrogen and possibly small hydrocarbons. These parasitic processes account for the almost constant background with ca. 5% relative intensity in Figure 1b. In positive mode we observe qualitatively the same behavior; however, the background signal is significantly larger (see Figure S2).

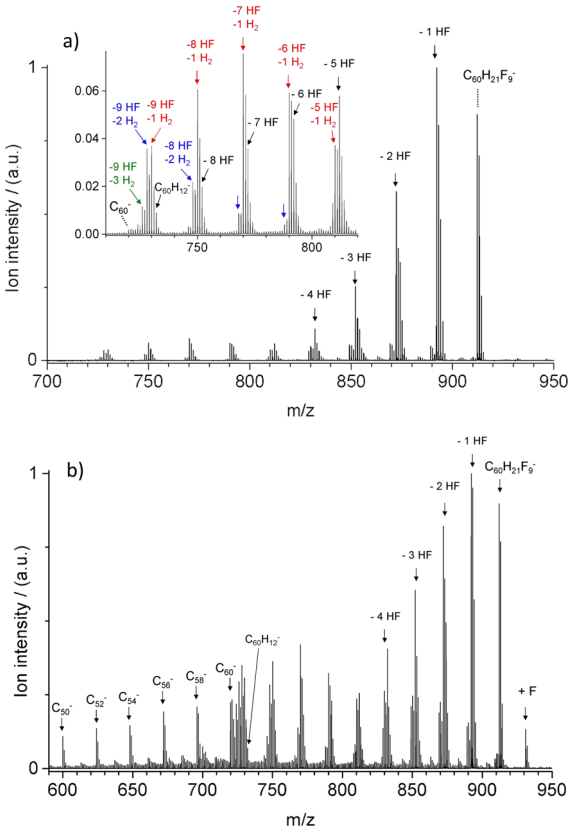

Figure 1. Negative ion mass spectra obtained upon laser-desorption of solid $C_{60}H_{21}F_9$: (a) low fluence (120 mJ/cm^2 per pulse) and (b) high fluence (150 mJ/cm^2). The dominant fragmentation channels are sequential HF-loss for the high mass fragments (black arrows) and a combination of HF-loss and H_2-loss for the lower mass fragments (colored arrows). Virtually no C_2-losses take place before C_{60} cage formation; at about 5% relative intensity, we observe an almost constant background.

The dominant HF/H_2-loss fragmentation behavior can be readily explained by a sequential "3-zipper" fragmentation mechanism as previously proposed (Figure 2):[1] in $C_{60}H_{21}F_9^-$, 6 fluorine atoms are in close proximity to hydrogen atoms (cove region), in favorable positions for synchronous HF-elimination. The HF-elimination and concomitant carbon−carbon bond formation is associated with the formation of either a new hexagonal or a new pentagonal carbon ring. This in turn leads to the induction of curvature in the $C_{60}H_{20}F_8^-$ fragment ion, and as a result, the next H···F-pair is formally moved into a cove region that is favorable for a further HF-elimination step. Thus, the HF-elimination procedure can be repeated until two hydrogen atoms come into close proximity. The prerequisite for this is that all three adjacent fluorine atoms (plus the three corresponding hydrogen atoms) on one of the three edges of the molecule have previously been removed; i.e., one of the three zippers must be fully closed before H_2-elimination can occur.

In order to determine whether HF-loss is preferred energetically over H_2-loss, we have estimated the fragmentation barrier for both processes. Since a computation of the transition states for each step of the $C_{60}H_{21}F_9^-$ fragmentation cascade is not feasible at the DFT-level, we have instead used benzo[c]-phenanthrene ($C_{18}H_{12}$) and 1-fluoro-benzo[c]phenanthrene ($C_{18}H_{11}F$) as simplified models.[1] These models basically represent one of the three lobes of $C_{60}H_{21}F_9$, see Figures 2

DOI: 10.1021/jacs.6b06205
J. Am. Chem. Soc. 2016, 138, 11254−11263

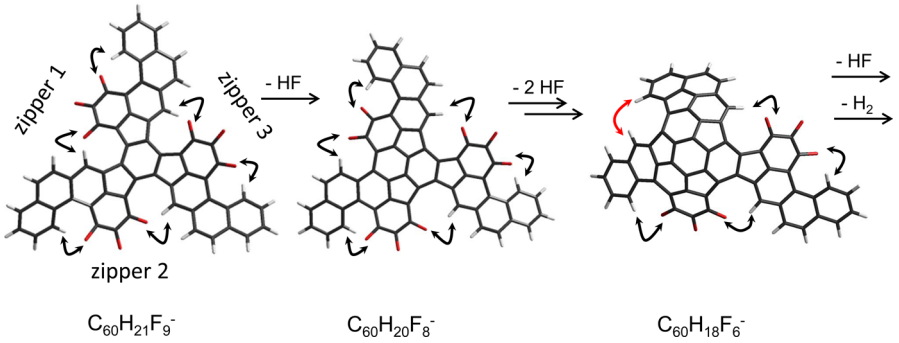

Figure 2. Schematic illustrating the two low energy fragmentation channels HF- and H_2-loss (terminal F atoms are indicated in red whereas H terminations are shown in gray). Possible fragmentation positions are marked by black (HF-loss) and red arrows (H_2-loss), respectively. Note that the isomer shown here for $C_{60}H_{18}F_6^-$ is not the global minimum, see Table 1 and Supporting Information.

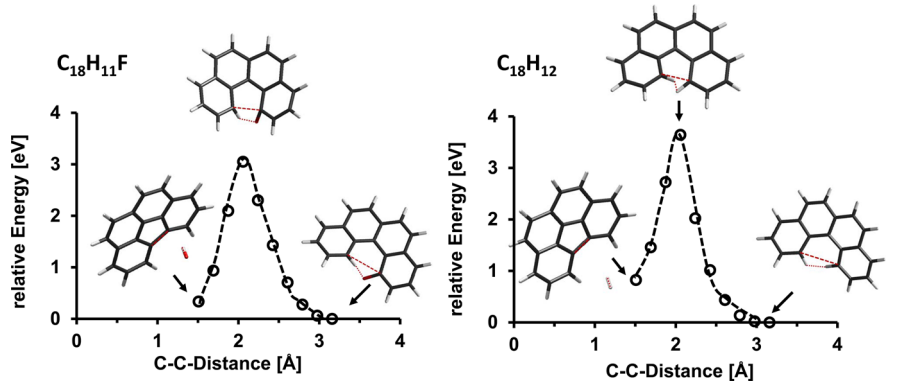

Figure 3. Estimation of the barrier height for HF- and H_2-loss and formation of a new carbon−carbon bond. Starting from the optimized structure of benzo[*c*] phenanthrene (DFT, BP86) and its fluorinated derivative. The carbon−carbon distance (and simultaneously the H−H/H−F distance) is systematically decreased while the remaining degrees of freedom are optimized. See text for details.

and 3. H_2 abstraction in $C_{18}H_{12}$ leads to $C_{18}H_{10}$ with the associated formation of a carbon−carbon bond leading to a new pentagonal ring. The analogous HF-loss is calculated for $C_{18}H_{11}F$, which has essentially the same geometric parameters. In both cases we first performed a full geometry optimization (DFT, BP86, def-svp basis, see above) of the parent molecules and then of the fragments $C_{18}H_{10}$ and H_2 (or HF). Note that these calculations were performed without any symmetry restrictions; i.e., all degrees of freedom were taken into account. The corresponding differences in total energy were found to be 0.82 eV ($C_{18}H_{12} \rightarrow C_{18}H_{10} + H_2$) and 0.56 eV ($C_{18}H_{11}F \rightarrow C_{18}H_{10} + HF$); i.e., both reactions are endothermic. Note, however, that the reactions are entropically favored; i.e., at high temperatures the reaction free energy will become negative. In order to estimate the barrier, we simultaneously interpolated both the C−C and the H−H (H−F) distances between parent's and fragments' structures (see Figure 3, red dotted lines) and optimized the remaining degrees of freedom. This is expected to yield a reasonable relative estimate of the two transition states. For the reaction $C_{18}H_{12} \rightarrow C_{18}H_{10} + H_2$, we obtain a barrier of 3.5 eV. For $C_{18}H_{11}F \rightarrow C_{18}H_{10} + HF$ we find a barrier of 3.0 eV. This is in reasonable agreement (taking into account differences in functional and basis set used) with the calculation of ref 1 who obtains a barrier of 3.48 eV for HF-loss (DFT, B3LYP). Apparently in this model system, both HF-loss and H_2-loss have similar and rather small barriers, with the barrier for HF-loss being 0.5 eV lower. A barrier height of 3−3.5 eV is significantly lower than the typical barrier height for carbon atom loss and C−C rearrangements and supports the proposed fragmentation mechanism. Note that H_2-loss can also take place via a radical mechanism which is not as selective.[15] The barrier for C_{Ar}−H bond cleavage in this two-step process is around 4.8 eV. Note further that HF-elimination can only be realized via a synchronous process. This represents a big advantage over HCl- and HBr-elimination (of the corresponding chlorinated or brominated derivatives) which takes place exclusively via the radical mechanism. On the basis of the same procedure (simultaneous interpolation of C−C and H−F distances and optimization of the remaining degrees of freedom), we have also estimated the transition state for the two HF-loss channels of $C_{60}H_{21}F_9^-$ leading to six- and five-ring formation, respectively. We obtain similar barrier heights of 2.7 and 2.9 eV, see Figure S3.

In order to assign the actual intermediate structures and ultimately confirm (or rule out) the formation of fullerene monoanions by laser-desorption of $C_{60}H_{21}F_9$, we determined the arrival time distribution (ATD) for each anionic fragment species generated (cf., Figure 1). As a general trend we observe a decrease in the arrival time with decreasing mass. It can be seen from Figure 4c (which provides a color-coded contour plot of arrival time distributions versus mass-to-charge ratios) that with decreasing mass the arrival times of the dominant fragments tend toward the arrival time of fullerene-C_{60} anion (see Figure S4 for trajectory-based ATDs). As already suggested by their characteristic C_2-loss fragmentation pattern, the ATDs confirm that even smaller fullerene fragments C_{60-2n}^- are generated (see Figure 4b) (with ATDs identical

DOI: 10.1021/jacs.6b06205
J. Am. Chem. Soc. 2016, 138, 11254−11263

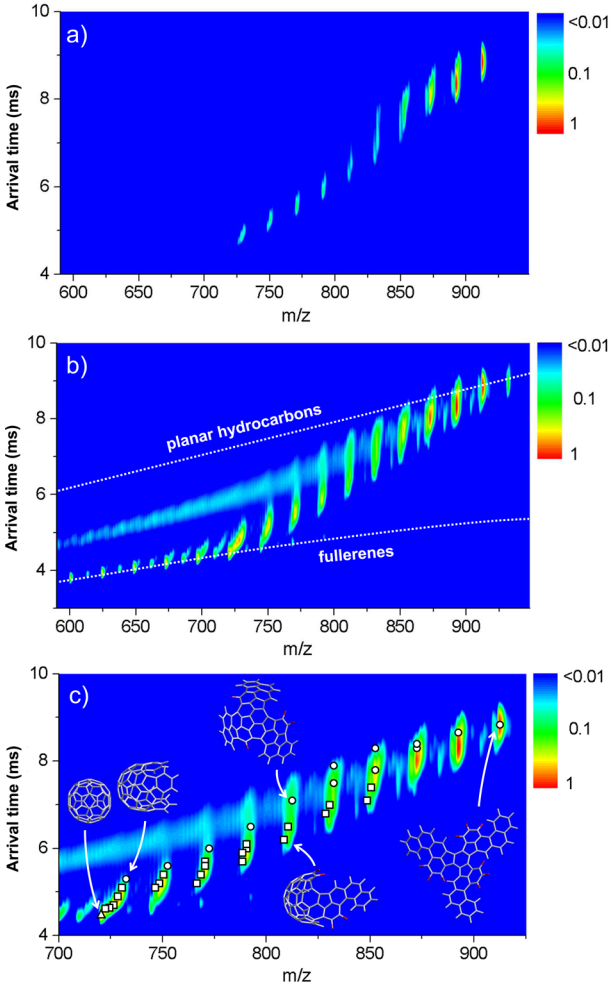

Figure 4. Contour plot of the arrival times versus masses of the monoanionic species (parent and fragment ions) obtained upon laser-desorption of solid $C_{60}H_{21}F_9$ at fluences of (a) 120 and (b) 150 mJ/cm^2. The dotted curves correspond to the calculated arrival times for fullerenes and planar hydrocarbons, respectively. (c) Comparison with calculated arrival times for various model structures (based on the projection approximation, PA). The circles correspond to $C_{60}H_{21-x}F_{9-x}^-$ ions (x = 0–9), i.e., sequential HF-loss; the squares correspond to additional hydrogen loss, $C_{60}H_{21-x-2y}F_{9-x}^-$ (y = 0–5). The triangle corresponds to the arrival time of fullerene C_{60}^-.

to the arrival time of the fragments of fullerene C_{60}^-, see Figure S1).

Besides fullerenes, we also observe trace amounts of other low mass species (low laser power, <1% relative peak height, see Figure 1a; high laser power, <5% relative peak height, see Figure 1b) with significantly larger arrival times (faint upper branch between m/z = 650–800 with arrival times between 5 and 6 ms, see Figure 4a) which we attribute to nonspherical structures. These species show a quite uniform mass distribution (see Figure 1b). We tentatively ascribe these trace species to secondary fragments arising from high energy isomers of $C_{60}H_{21-x-y}F_{9-x}^-$, i.e., to species whose topology prevents them from achieving fullerene cage closure. Note that the mass spectra indicate that, in addition to H_2-loss, some H-loss processes compete with the HF-elimination. When the cleavage of the C–H bond takes place without a C_{Ar}–F group in the vicinity, no new C–C bond can be expected to form. The product of such a step is a highly reactive radical anion which may be able to undergo Stone–Wales-like rearrangement leading to the transfer of pentagons to the molecular periphery (favorable thermodynamically). Moreover, removal of H atoms from the immediate vicinity of a C–F termination blocks the channel for HF-elimination at that position. Consequently, the ensuing fragments remain more planar (with surviving F atoms); i.e., pathways toward closed C_{60} cages are blocked. Overall fullerene anion yields could be further reduced by thermally activated electron autodetachment processes which would transfer some of the population away from the anion channel into (nondetectable) neutral congeners. Finally, it is also worth noting that traces (less than 5%) of "wrongly" connected precursor (with some F atoms located in positions unsuitable for direct HF-elimination) are present in the $C_{60}H_{21}F_9$ precursor (see Figure S5). These would initially fragment by H_2-elimination leading to planar species which can no longer follow the "golden line" to C_{60}^-.

In order to shed more light on the primary fragmentation cascade as observed in experiment, we performed full geometry optimizations of representative anionic fragments that are in line with the "zipper" fragmentation scheme as first proposed in ref 15. The resulting structures which correspond to the lowest energy isomers found at each composition are summarized in Table 1 and Figures 5 and 6. A complication in the search for minimum-energy species is the occurrence of multiple isomers at essentially each step in the cascade. Fragmentation of $C_{60}H_{21}F_9^-$ via HF-loss can occur at six different positions (see Figure 2), three of which are identical due to the 3-fold symmetry of $C_{60}H_{21}F_9$ resulting in two distinguishable $C_{60}H_{20}F_8^-$ fragments. One of these contains an additional hexagonal ring (see Table 1 and Figure S6, isomer 1), the other a pentagon (isomer 2). On the basis of the calculated total energies we find that isomer 1 is favored by 0.3 eV. Both fragmentation channels are endoergic by 0.49 and 0.79 eV, respectively (calculated as the difference of DFT energies between the respective $C_{60}H_{20}F_8^-$ isomer plus HF and $C_{60}H_{21}F_9^-$ (without considering zero point energies)). We estimate the barrier to be significantly higher than the energy difference between the channels, see above. This implies that under our experimental conditions both fragmentation channels are likely to be active. On the basis of their very similar ion mobilities we cannot differentiate between the two isomers experimentally; both have a PA-CCS of 226 Å^2, which translates into a calculated arrival time of 8.7 ms. This is somewhat larger than the arrival time maximum observed for $C_{60}H_{20}F_8^-$ (8.3 ms, see Figure 4b) but within our 5% error limit.

In the next fragmentation step, HF-loss from the two isomers of $C_{60}H_{20}F_8^-$ can give rise to eight topologically different isomers of $C_{60}H_{19}F_7^-$ (for a complete list, see Figure S7). These correspond to either the same zipper being closed, either to the left or to the right of the initially formed hexagon, or to HF-loss at one of the other two sides/zippers of the molecule. Most of these eight isomers are within 1 eV of the lowest energy form, with one exception: isomer 8 (+5.7 eV). In this case an energetically highly unfavorable 4-membered- ring is formed (see Figure 4 and Figure S8). The PA-CCS values of the low energy isomers cover a range from 210 to 222 Å^2, corresponding to arrival times of 8.06–8.52 ms. This agrees with the observed arrival time for $C_{60}H_{19}F_7^-$ within the 5% error limit, see Figure 4.

Each of the eight possible $C_{60}H_{19}F_7^-$ isomers has six different possible ways to eliminate the third HF molecule. Therefore,

DOI: 10.1021/jacs.6b06205
J. Am. Chem. Soc. 2016, 138, 11254–11263

Table 1. Calculated Structures, Energies, and Collision Cross Sections[a]

	isomer no.	energy [a.u.]	rel energy [eV]	electron affinity [eV]	calcd cross section [Å^2]	calcd ATD [ms]
$C_{60}H_{21}F_9^-$	1	−3195.5513547	0	2.10	230 (235)	8.8 (8.8)
$C_{60}H_{20}F_8^-$	1	−3095.1886002	0	2.34	226 (226)	8.7 (8.5)
	2	−3095.1774156	0.30	2.03	226 (230)	8.7 (8.6)
$C_{60}H_{19}F_7^-$	1	−2994.8180953	0	2.45	219 (222)	8.4 (8.3)
	2	−2994.7995401	0.50	2.38	217 (223)	8.3 (8.3)
$C_{60}H_{18}F_6^-$	1	−2894.4383007	0	2.47	215 (216)	8.3 (8.1)
	2	−2894.4028740	0.96	2.39	205 (215)	7.8 (8.0)
$C_{60}H_{16}F_6^-$	1	−2893.1760599	0	2.36	194 (205)	7.4 (7.6)
$C_{60}H_{14}F_6^-$	1	−2891.9492947	0	2.46	187 (199)	7.1 (7.4)
$C_{60}H_{17}F_5^-$	1	−2794.0477269	0	2.46	207 (212)	7.9 (7.9)
	2	−2794.0372826	0.28	2.47	195 (208)	7.5 (7.8)
$C_{60}H_{15}F_5^-$	1	−2792.7904541	0	2.46	184 (196)	7.0 (7.3)
$C_{60}H_{13}F_5^-$	1	−2791.5737732	0	2.64	178 (188)	6.8 (7.0)
$C_{60}H_{16}F_4^-$	1	−2693.6452533	0	2.44	186 (202)	7.1 (7.5)
$C_{60}H_{14}F_4^-$	1	−2692.4077792	0	2.47	170 (180)	6.5 (6.7)
	2	−2692.4066340	0.03	2.35	172 (183)	6.5 (6.8)
$C_{60}H_{12}F_4^-$	1	−2691.1909569	0	2.66	164 (173)	6.2 (6.4)
	2	−2691.1796867	0.31	2.43	164 (174)	6.2 (6.4)
$C_{60}H_{15}F_3^-$	1	−2593.2514150	0	2.44	172 (184)	6.5 (6.8)
$C_{60}H_{13}F_3^-$	1	−2592.0289632	0	2.31	159 (166)	6.0 (6.1)
	2	−2592.0279504	0.03	2.49	163 (172)	6.2 (6.4)
$C_{60}H_{11}F_3^-$	1	−2590.8115638	0	2.64	157 (165)	5.9 (6.1)
	2	−2590.8005371	0.30	2.36	151 (158)	5.7 (5.8)
$C_{60}H_{14}F_2^-$	1	−2492.8613133	0	2.35	159 (168)	6.0 (6.2)
	2	−2492.8524649	0.24	2.30	158 (167)	6.0 (6.2)
$C_{60}H_{12}F_2^-$	1	−2491.6539811	0	2.48	151 (159)	5.7 (5.8)
$C_{60}H_{10}F_2^-$	1	−2490.4253051	0	2.54	143 (150)	5.4 (5.5)
$C_{60}H_8F_2^-$	1	−2489.1977703	0	2.52	137 (143)	5.2 (5.2)
$C_{60}H_{13}F^-$	1	−2392.4735828	0	2.29	149 (157)	5.6 (5.7)
	2	−2392.4654282	0.22	2.33	148 (156)	5.6 (5.7)
$C_{60}H_{11}F^-$	1	−2391.2661062	0	2.43	143 (149)	5.4 (5.4)
$C_{60}H_9F^-$	1	−2390.0566115	0	2.52	138 (144)	5.2 (5.2)
$C_{60}H_7F^-$	1	−2388.8494608	0	2.65	135 (140)	5.1 (5.1)
$C_{60}H_{12}^-$	1	−2292.0779284	0	2.30	140 (147)	5.3 (5.4)
$C_{60}H_{10}^-$	1	−2290.8704283	0	2.44	135 (141)	5.1 (5.1)
$C_{60}H_8^-$	1	−2289.6589825	0	2.48	130 (136)	4.9 (4.9)
$C_{60}H_6^-$	1	−2288.4803131	0	2.51	125 (129)	4.7 (4.7)
$C_{60}H_4^-$	1	−2287.2887624	0	2.55	123 (128)	4.6 (4.6)
	2	−2287.2757986	0.35	2.56	123 (128)	4.6 (4.6)
$C_{60}H_2^-$	1	−2286.0853499	0	2.65	122 (127)	4.6 (4.5)
	2	−2286.0690483	0.44	2.97	122 (127)	4.6 (4.5)
C_{60}^-	1	−2284.8882414	0	2.76	120 (125)	4.5 (4.5)

[a]All geometries are fully optimized as radical anions. The electron affinities are calculated as energy difference of the respective geometry optimized anion and neutral species. The numbers in parentheses correspond to the calculated cross sections and arrival times based on the trajectory method.

for $C_{60}H_{18}F_6^-$ and beyond, the number of "regular" isomers to be considered increases dramatically. As a consequence, it is not feasible to calculate them all, at least for the purposes of this publication. We have therefore considered two limiting cases.

1. Fragmentation Cascade Involving Nine Sequential HF-Losses Followed by Six Sequential H_2-Eliminations. To model this, we have first characterized a path to $C_{60}H_{12}^-$ which proceeds in nine individual HF-elimination steps each with the lowest possible endoergicities at the corresponding point in the sequence. Proceeding further from the $C_{60}H_{12}^-$ isomer generated in this fashion, we have then analogously characterized the continued path to C_{60}^- [via the sequence of six lowest endoergicity H_2-elimination steps (see Figure 5 and Figure S9)]. In each of the total of 15 elimination steps the endoergicity remains below 1.5 eV. In most cases, the cascade follows the lowest energy "representative" structures that we had found previously for $C_{60}H_{21-x-y}F_{9-x}^-$ by inspection/chemical intuition [these isomers are indicated as (1) in Table 1 (and Figure 5)]. As a general trend, we observe that the three "zippers" close at the same rate. In other words, the first three elimination steps involve HF molecules whose constituent atoms occupied initially equivalent positions on each of the three sides. The next three elimination steps again involve H/F atoms initially occupying equivalent positions on each of the three sides, thereby maximizing the distance between the remaining fluorine atoms. It is also noteworthy that in this transformation path the carbon cage closes [to the $C_{60}(I_h)$ connectivity] already at $C_{60}H_6^-$.

The cross sections that we obtain from these calculations are indicated as circles in Figure 4c. They are at the upper limit of

DOI: 10.1021/jacs.6b06205
J. Am. Chem. Soc. 2016, 138, 11254−11263

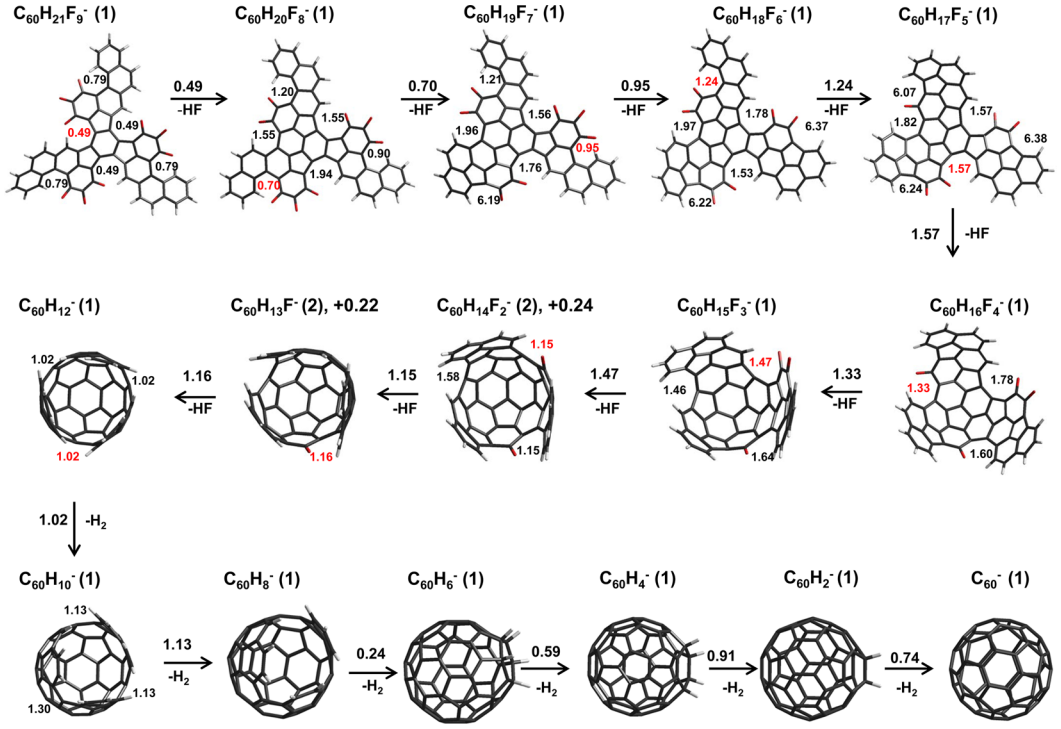

Figure 5. Calculated low energy structures for each step of the fragmentation cascade leading from $C_{60}H_{21}F_9^-$ to C_{60}^- via nine sequential HF-eliminations followed by six H_2-loss steps. Numbers (in eV) given above the arrows drawn between structures correspond to the endoergicities of each fragmentation step (*not* their activation energies). The smaller numbers shown adjacent to the individual molecule representations indicate the endoergicity of a cyclodehydrohalogenation/cyclodehydrogenation reaction at that specific location. Red numbers indicate the lowest energy elimination step of those possible at that point in the fragmentation sequence. In most cases the cascade shown follows the lowest energy structures (numbered 1 in Table 1) found for each anionic species along the fragmentation path, with two exceptions where the second lowest energy isomers (2) are shown together with their energy offsets from 1. See text.

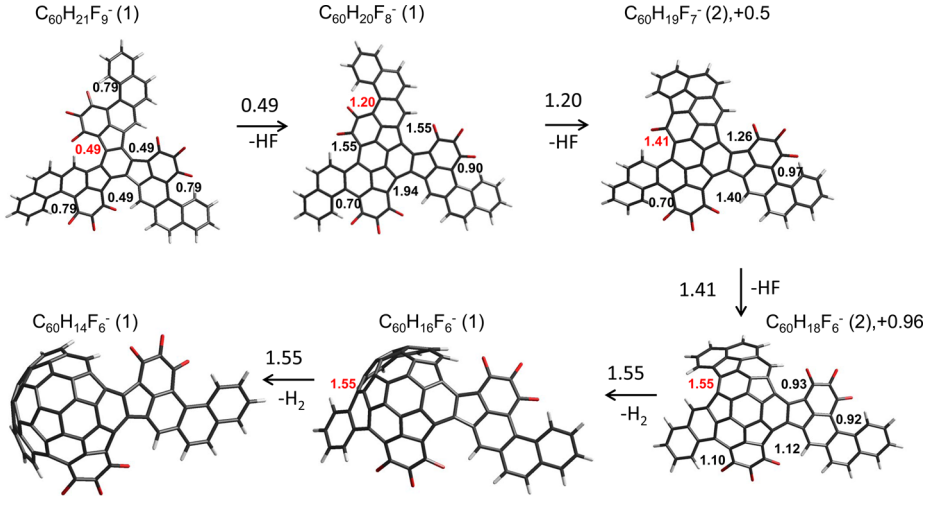

Figure 6. Lowest energy structures and energetics for an assumed 3HF-loss + $2H_2$-loss sequence to form $C_{60}H_{14}F_6^-$. Again, the numbers correspond to the energy differences (in eV) between the respective parent and fragment ions, i.e., the endoergicity in each step (*not* the activation energy). The red numbers indicate the fragmentation/elimination reaction that leads to the next structure in the sequence.

the experimental data. Obviously, this (9HF + $6H_2$)-elimination cascade, albeit energetically favored, is not the only one observed experimentally. In the mass spectra (Figure 1) we can also observe a combination of HF- and H_2-losses, already in the early steps of the fragmentation cascade. Consequently, we have also calculated a second generic type of fragmentation cascade.

2. Fragmentation Cascade Incorporating Early H_2-Losses. We model this scenario by assuming a (HF + HF + HF + H_2 + H_2)-loss path; see Figure 6 which shows the first five steps of the assumed fragmentation sequence. This requires that the first three HF molecules are removed from the same side of the molecule; i.e., only one zipper closes, leading to a $C_{60}H_{18}F_6^-$ isomer (isomer 2, see Table 1) which is 0.96 eV higher in energy than the (lowest energy) isomer observed in the first cascade. However, from step to step the endoergicity still remains below 1.5 eV, i.e., not dramatically higher than for the "energetically-preferred-at-each-step" 9HF + $6H_2$ cascade

DOI: 10.1021/jacs.6b06205
J. Am. Chem. Soc. 2016, 138, 11254−11263

(see case 1 above). Once formed, this $C_{60}H_{18}F_6^-$ isomer can fragment via H_2-loss with an endothermicity of 1.55 eV (compared to 0.92−1.12 eV for HF-loss). Therefore, it seems plausible that both limiting cases of the fragmentation cascade (and combinations thereof) can proceed in parallel under the laser-desorption ionization conditions used. The resulting hydrogen deficient species $C_{60}H_{21-x-2y}F_{9-x}^-$ are indicated as squares in Figure 4c and summarized in Table 1. Note that all of the different H_2-, HF-loss sequences considered finally lead to the icosahedral fullerene-C_{60} cage without the need for highly energetic C−C rearrangements. The calculated (DFT, BP86) total energy difference ($C_{60}H_{21}F_9^- \rightarrow C_{60}^- + 9$ HF + 6 H_2) adds up to 14.7 eV; i.e., the average endoergicity per fragmentation step is slightly below 1 eV [for comparison, the endoergicity for the fragmentation of C_{60}^- to C_{58}^- by C_2-loss is much higher, on the order of 11.1 eV (DFT, BP-86, def-svp basis set)].

As can be seen from Figure 4c, the experimental and calculated collision cross section values agree to within 5% for all fragment species; i.e., our calculations can reproduce the characteristic experimental ATD versus mass pattern observed in the anion channel upon laser-desorption of solid $C_{60}H_{21}F_9$ (Figure 4c, circles and squares). This level of agreement allows us to set narrow bounds on the actual molecular structures passed through along the fragmentation cascade and, as a result, to obtain representative "freeze-frame" images of the transformation of a hot near-planar F-PAH precursor into a 60 atom carbon cage in a sequence of 15 fragmentation steps which can be completed within a few microseconds after desorption.

As discussed above, laser-desorption of a solid $C_{60}H_{21}F_9$ sample gives rise to a fragment mass spectrum which can be explained in terms of numerous 15 step unimolecular dissociation cascades occurring in parallel. All of these transform $C_{60}H_{21}F_9$ to C_{60}^- via loss of a total of 9 HF and 6 H_2 molecules (in many different sequences). In previous work focusing on the thermal stability of solid $C_{60}H_{21}F_9$, we have demonstrated that up to three of these sequential HF-elimination steps can already be induced on-surface simply by heating.[3] Therefore, it is possible that, besides unimolecular fragmentation in gas the phase, on-surface reactions (e.g., as mediated by a previous laser pulse) could also be contributing to the fullerene anion signals observed here. Specifically, recombination of smaller polycyclic fragments either on-surface or in the high density region of the desorption plume might be involved. In order to resolve this question we have mass selected the ions generated by laser-desorption and have then probed their (argon) collision-induced dissociation (CID) by ion mobility mass spectrometry (see Experimental Methods). At near zero collision energy (4 a.u.), $C_{60}H_{21}F_9^-$ passes the cell without any measurable fragmentation (see Figure 7a and Figure S10a). Upon increasing the collision energy to 60 a.u., $C_{60}H_{21}F_9^-$ starts to fragment predominantly via loss of up to three HF-units (see Figure 7b and Figure S10b). At a collision energy of 100 a.u. (Figure 7c and Figure S10c), we observe basically the complete HF-loss cascade leading from $C_{60}H_{21}F_9^-$ all the way down to $C_{60}H_{12}^-$. It is also worth noting that under these CID conditions the arrival time distribution is broadest in the mass range corresponding to predominantly 5 HF-losses (m/z = 812 ± 2), while it is much narrower for both larger and smaller fragments. This is fully in line with the proposed fragmentation mechanism (see above): in the middle of the fragmentation cascade we expect a large number of different isomers (with different CCS and therefore different arrival

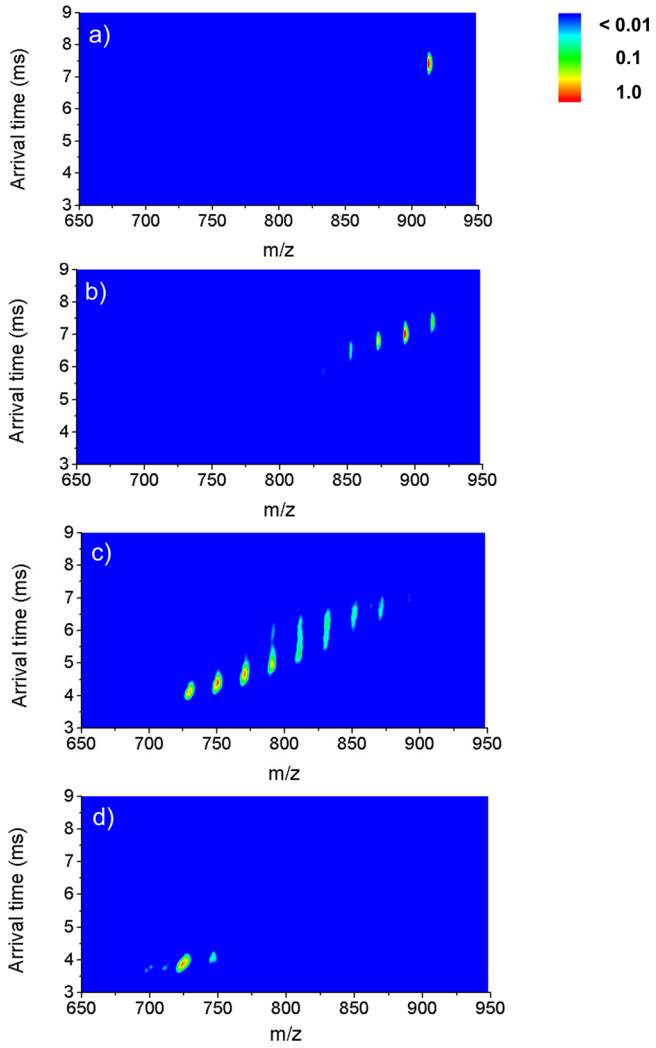

Figure 7. Contour maps of anion signal versus arrival time and mass obtained upon collision-induced-dissociation of mass-selected $C_{60}H_{21}F_9^-$: The parent ion (m/z = 912) is mass selected prior to injection into an argon filled collision gas cell. Fragment ion mass distributions and corresponding ion mobilities are determined as a function of the collision energy. (a) Collision energy 4 a.u.: only the parent ion is observed. (b) Collision energy 60 a.u.: three fragmentation steps (HF-losses) are observed. (c) Collision energy 100 a.u.: nine fragmentation steps (HF-losses) are observed. The spectrum is dominated by $C_{60}F_nH_{12+n}^-$, $n < 3$. (d) Collision energy 200 a.u.: C_{60}^-, the end product of the fragmentation cascade (HF-loss, followed by H_2-loss), can be observed. All contour maps are normalized to the highest signal intensity within the regions shown. Note that, due to the different TWIMS conditions, the arrival times of the different species cannot be compared with those shown in Figure 4.

times) while at the beginning and the end of the cascade only a very limited number of isomers is possible. Finally, at the highest collision energy of 200 a.u. we observe complete fragmentation down to $C_{60}H_x^-$ ($x \leq 12$), including fullerene-C_{60}^- (Figure 7d and Figure S10d). In a variant of this experiment (see Figure S11), we have also isolated and fragmented $C_{60}H_{12}^-$ (produced as a fragmentation product during laser-desorption of $C_{60}H_{21}F_9$): at high collision energy it fragments to C_{60}^- and even further to C_{58}^-. To summarize, this proves that fullerene-C_{60} is formed primarily by the proposed 15 step unimolecular fragmentation mechanism *in the gas phase*,

DOI: 10.1021/jacs.6b06205
J. Am. Chem. Soc. 2016, 138, 11254−11263

without the need to invoke a recombination of fragments or other laser-induced on-surface transformation process.

SUMMARY

We have studied the cascade of unimolecular fragmentation steps induced by laser-desorption/ionization of solid $C_{60}H_{21}F_9$. By using a combination of anion mass spectrometry, ion mobility mass spectrometry, and quantum chemical calculations (to generate structural models and to determine their ground state properties), we have been able to set narrow bounds on the structures of the fragment ions accessed. Our results support previous inferences that the dominant decay process for thermally activated $C_{60}H_{21}F_9^-$ comprises a sequence of regioselective cyclodehydrofluorination and cyclodehydrogenation reactions. We confirm the "three zippers" sequential fragmentation mechanism, involving sequential HF- and H_2-loss (and concomitant pentagon and hexagon ring formation) which transforms the near-planar parent species into a series of structures with increased curvature and finally to C_{60}^-. This species is found to be a closed-shell carbon cage.

While the mere detection of fullerene anions after a 15 step sequence of unimolecular dissociations indicates that the branching ratios for competing reactions must be quite low, overall fullerene yields could clearly be improved further. As a first step this requires accurate experimental determinations of activation energies and quantitative kinetic modeling. In future work it will then become interesting to explore to what extent the overall yield of C_{60}^- can be enhanced by controlling the energization rate and corresponding internal energy distributions, e.g., via resonant laser excitation. Performing such experiments in an ion trap (or flow tube reactor in the case of sublimable neutrals) may allow an online fine-tuning of branching ratios thus yielding a "fragmentation temperature program" to match the preprogrammed structure. More generally, being able to make higher fullerenes, non-IPR fullerenes, and heterofullerenes in high yield via multiple sequential unimolecular HF-eliminations will depend in large part on how well the corresponding reaction kinetics can be controlled step-by-step.

ASSOCIATED CONTENT

Supporting Information

The Supporting Information is available free of charge on the ACS Publications website at DOI: 10.1021/jacs.6b06205.

Additional figures including mass spectra, contour maps of anion signal versus arrival time and mass, and structures, and experimental parameters (PDF)

AUTHOR INFORMATION

Corresponding Authors

*konstantin.amsharov@fau.de

*manfred.kappes@kit.edu

Notes

The authors declare no competing financial interest.

ACKNOWLEDGMENTS

M.M.K. acknowledges support of this research by (i) Helmholtz program POF-STN, (ii) Karlsruhe Nano Micro Facility (KNMF), and (iii) KIT/Land Baden-Württemberg. J.-F.G. acknowledges support by the Hector Fellow Academy. K.Yu.A. acknowledges financial support from Deutsche Forschungsgemeinschaft.

REFERENCES

(1) Amsharov, K. Y.; Kabdulov, M. A.; Jansen, M. *Chem. - Eur. J.* **2010**, *16*, 5868−5871.

(2) Amsharov, K. Y.; Kabdulov, M. A.; Jansen, M. *Eur. J. Org. Chem.* **2009**, 6328−6335.

(3) Ulas, S.; Weippert, J.; Amsharov, K. Y.; Jansen, M.; Pop, M. L.; Diudea, M. V.; Strelnikov, D.; Böttcher, A.; Kappes, M. M. *J. Phys. Chem. C* **2015**, *119*, 7308−7318.

(4) Wentrup, C. *Aust. J. Chem.* **2014**, *67*, 1150−1165.

(5) Tsefrikas, V. M.; Scott, L. T. *Chem. Rev.* **2006**, *106*, 4868−4884.

(6) Amsharov, K. Y.; Abdurakhmanova, N.; Stepanow, S.; Rauschenbach, S.; Jansen, M.; Kern, K. *Angew. Chem., Int. Ed.* **2010**, *49*, 9392−9396.

(7) Sanchez-Valencia, J. R.; Dienel, T.; Gröning, O.; Shorubalko, I.; Mueller, A.; Jansen, M.; Amsharov, K. Y.; Ruffieux, P.; Fasel, R. *Nature* **2014**, *512*, 61−64.

(8) Koolen, H. H. F.; Klitzke, C. F.; Cardoso, F. M. R.; Rosa, P. T. V.; Gozzo, F. C. *J. Mass Spectrom.* **2016**, *51*, 254−256.

(9) Santos, V. G.; Fasciotti, M.; Pudenzi, M. A.; Klitzke, C. F.; Nascimento, H. L.; Pereira, R. C. L.; Bastos, W. L.; Eberlin, M. N. *Analyst* **2016**, *141*, 2767−2773.

(10) (a) Cami, J.; Bernard-Salas, J.; Peeters, E.; Malek, S. E. *Science* **2010**, *329*, 1180−1182. (b) Campbell, E. K.; Holz, M.; Gerlich, D.; Maier, J. P. *Nature* **2015**, *523*, 322−323. (c) Strelnikov, D.; Kern, B.; Kappes, M. M. *Astron. Astrophys.* **2015**, *584*, A55. (d) Zhen, J.; Castellanos, P.; Paardekooper, D. M.; Linnartz, H.; Tielens, A. G. G. M. *Astrophys. J., Lett.* **2014**, *797*, L30.

(11) (a) Scott, L. T. *Pure Appl. Chem.* **1996**, *68*, 291−300. (b) Plater, M. J.; Praveen, M.; Schmidt, D. M. *Fullerene Sci. Technol.* **1997**, *5*, 781−800.

(12) (a) Boorum, M. M.; Vasil'ev, Y. V.; Drewello, T.; Scott, L. T. *Science* **2001**, *294*, 828−831. (b) Scott, L. T.; Boorum, M. M.; McMahon, B. J.; Hagen, S.; Mack, J.; Blank, J.; Wegner, H.; de Meijere, A. *Science* **2002**, *295*, 1500−1503.

(13) (a) Amsharov, K. Y.; Jansen, M. *Chem. Commun.* **2009**, *19*, 2691−2693. (b) Amsharov, K. Y.; Jansen, M. *J. Org. Chem.* **2008**, *73*, 2931−2934.

(14) Kabdulov, M. A.; Amsharov, K. Y.; Jansen, M. *Tetrahedron* **2010**, *66*, 8587−8593.

(15) (a) Scott, L. T. *Angew. Chem., Int. Ed.* **2004**, *43*, 4994−5007. (b) Tsefrikas, V. M.; Scott, L. T. *Chem. Rev.* **2006**, *106*, 4868−4884. (c) Thilgen, C. *Angew. Chem., Int. Ed.* **2012**, *51*, 7082−7084.

(16) Amsharov, Y. K.; Kabdulov, M. A.; Jansen, M. *Angew. Chem., Int. Ed.* **2012**, *51*, 4594−4597.

(17) Kabdulov, M.; Jansen, M.; Amsharov, K. Y. *Chem. - Eur. J.* **2013**, *19*, 17262−17266.

(18) Amsharov, K. Y.; Abdurakhmanova, N.; Stepanow, S.; Rauschenbach, S.; Jansen, M.; Kern, K. *Angew. Chem., Int. Ed.* **2010**, *49*, 9392−9396.

(19) Rim, K. T.; Siaj, M.; Xiao, S. X.; Myers, M.; Carpentier, V. D.; Liu, L.; Su, C. C.; Steigerwald, M. L.; Hybertsen, M. S.; McBreen, P. H.; Flynn, G. W.; Nuckolls, C. *Angew. Chem., Int. Ed.* **2007**, *46*, 7891−7895.

(20) Otero, G.; Biddau, G.; Sanchez-Sanchez, C.; Caillard, R.; Lopez, M. F.; Rogero, C.; Palomares, F. J.; Cabello, N.; Basanta, M. A.; Ortega, J.; Mendez, J.; Echavarren, A. M.; Perez, R.; Gomez-Lor, B.; Martin-Gago, J. A. *Nature* **2008**, *454*, 865−867.

(21) Abdurakhmanova, N.; Mueller, A.; Stepanow, S.; Rauschenbach, S.; Jansen, M.; Kern, K.; Amsharov, K. Y. *Carbon* **2015**, *84*, 444−447.

(22) (a) Giles, K.; Pringle, S. D.; Worthington, K. R.; Little, D.; Wildgoose, J. L.; Bateman, R. H. *Rapid Commun. Mass Spectrom.* **2004**, *18*, 2401−2414. (b) Ruotolo, B. T.; Giles, K.; Campuzano, I.; Sandercock, A. M.; Bateman, R. H.; Robinson, C. V. *Science* **2005**, *310*, 1658−1661.

(23) Pringle, S. D.; Giles, K.; Wildgoose, J. L.; Williams, J. P.; Slade, S. E.; Thalassinos, K.; Bateman, R. H.; Bowers, M. T.; Scrivens, J. H. *Int. J. Mass Spectrom.* **2007**, *261*, 1−12.

(24) Furche, F.; Ahlrichs, R.; Hättig, C.; Klopper, W.; Sierka, M.; Weigend, F. *WIREs Comput. Mol. Sci.* **2014**, *4*, 91−100.

DOI: 10.1021/jacs.6b06205
J. Am. Chem. Soc. 2016, 138, 11254−11263

(25) Becke, A. D. *Phys. Rev. A: At., Mol., Opt. Phys.* **1988**, *38*, 3098−3100.
(26) Perdew, J. P. *Phys. Rev. B: Condens. Matter Mater. Phys.* **1986**, *33*, 8822−8824.
(27) Weigend, F.; Ahlrichs, R. *Phys. Chem. Chem. Phys.* **2005**, *7*, 3297−3305.
(28) von Helden, G.; Hsu, M.-T.; Gotts, N.; Bowers, M. T. *J. Phys. Chem.* **1993**, *97*, 8182−8192.
(29) Shvartsburg, A. A.; Jarrold, M. F. *Chem. Phys. Lett.* **1996**, *261*, 86−91.
(30) Mesleh, M. F.; Hunter, J. M.; Shvartsburg, A. A.; Jarrold, M. F.; Schatz, G. C. *J. Phys. Chem.* **1996**, *100*, 16082−16086.

DOI: 10.1021/jacs.6b06205
J. Am. Chem. Soc. 2016, 138, 11254−11263